



Photoactive g-C₃N₄/CuZIF-67 bifunctional electrocatalyst with staggered p-n heterojunction for rechargeable Zn-air batteries

Ren Ren^a, Guicheng Liu^{b,*}, Ji Young Kim^a, Ryanda Enggar Anugrah Ardhi^a, Minh Xuan Tran^a, Woochul Yang^b, Joong Kee Lee^{a,**}

^a Energy Storage Center, Clean Energy Institute, Korea Institute of Science and Technology (KIST), Hwarang-ro 14-gil 5, Seongbuk-gu, Seoul 02792, Republic of Korea

^b Department of Physics, Dongguk University, Seoul 04620, Republic of Korea

ARTICLE INFO

Keywords:

Photo-enhanced electrocatalyst
Staggered p-n heterojunction
Durability
ORR/OER
Rechargeable Zn-air battery

ABSTRACT

Energy level matching and structural stabilization of semiconductor electrode materials are critical for improving the efficiency and durability of bifunctional catalysts for photo-enhanced rechargeable Zn-air batteries. We developed a photoactive bifunctional air-electrocatalyst comprising n-type g-C₃N₄ and p-type copper-doped ZIF-67 (CuZIF-67) composite. g-C₃N₄/CuZIF-67 exhibits wide-range solar spectrum absorption and enhanced electron-hole pairs separation efficiency owing to synergistic effects of a suitable bandgap width, staggered p-n heterojunction band gap structure, and built-in electric field at its p-n heterojunction, leading to higher oxygen evolution reaction (OER) and oxygen reduction reaction (ORR) activities compared with single p- and n-type catalysts. It has photo-enhanced charge/discharge abilities, has a voltage gap of 0.81 V under 1-sun-illumination, and maintains stable cycling with 60% round-trip efficiency under illumination over 1000 cycles for 336 h at 2 mA cm⁻². In conclusion, staggered p-n heterojunction and pyrrolic nitrogen-rich groups are important for efficient and durable photo-enhanced Zn air batteries.

1. Introduction

Rechargeable zinc-air batteries (RZBs) demonstrate significant potential as next-generation batteries, as they are non-flammable, resource-abundant, cost-efficient, feasible for ambient air operation, and have remarkable theoretical energy density (1086 Wh kg⁻¹) [1–6]. However, the development of RZBs needs to address many challenges to speed up their commercialization [7,8]. For example, low round-trip efficiency during cycling is caused by the retarded reactivity of the oxygen reduction reaction (ORR) and oxygen evolution reaction (OER) at the air cathode [9–12]. An air cathode with deficient electrocatalytic kinetics creates a large voltage gap, especially when the practical charge voltage is >2.0 V, during the charging and discharging process [13,14]. Moreover, RZBs have a limited cycle life owing to the structural degradation of air cathodes working under high charge voltage [15,16]. Therefore, it is essential to improve both the round-trip efficiency and structural durability of air cathodes to ensure further development and commercialization of RZBs.

For efficient energy generation and storage, photo-enhanced RZBs

that combine photochemical and electrochemical energy conversion and storage with the help of solar energy, are a promising research focus [17]. Photo-enhanced RZBs require a photoactive OER/ORR bifunctional cathode that is not merely an electrochemical catalyst but also a photo-active catalyst. To improve the utilization efficiency of solar power, semiconductor photoelectrodes with a wide-range solar spectrum absorption ability and a heterojunction with effective hole-pair separation are preferred for constructing photo-enhanced RZBs [18, 19]. In other words, a semiconductor band gap of 1.7–2.9 eV is optimal for absorbing photons from sunlight owing to the high concentration of sunlight in the visible light wavelength range from 420 to 700 nm [20]. At present, the photocatalytic efficiency of individual semiconductors is limited by fast electron-hole recombination and deficient visible light utilization [21]. The use of more than one semiconductor with different band gaps to form properly engineered heterojunction photocatalysts is expected to improve photocatalytic activity owing to optimized electron-hole separation efficiency and extended light absorption range. Unfortunately, research on photoactive materials for photo-enhanced RZBs is limited and focused on single semiconductor photoactive

* Corresponding author.

** Corresponding author.

E-mail addresses: log67@163.com, liuguicheng@dongguk.edu (G. Liu), leejk@kist.re.kr (J.K. Lee).

<https://doi.org/10.1016/j.apcatb.2022.121096>

Received 12 October 2021; Received in revised form 16 December 2021; Accepted 9 January 2022

Available online 10 January 2022

0926-3373/© 2022 Elsevier B.V. All rights reserved.

electrocatalysts, for example, p-type Co_3O_4 [13], p-type polythiophene [18], and n-type BiVO_4 [15].

Based on the location of the conduction band (CB) and valence band (VB), heterojunction materials are categorized into the straddling gap, staggered gap, and broken gap structures [21]. Among these, the staggered gap is the preferred heterojunction structure to enhance photocatalytic performance owing to its suitable band gap structure for the spatial separation of photo-generated electron-hole pairs [22,23]. Although staggered gap heterojunctions can separate electron-hole pairs, the enhanced electron-hole separation efficiency is not adequate for ultrafast electron-hole recombination on the interface of semiconductors. Therefore, p-n heterojunctions, combinational p- and n-type semiconductors with unequal band gaps, are the most suitable systems for accelerating electron-hole migration across heterojunctions during the charge/discharge process, consequently improving RZB performance by providing an additional electric field [24]. In staggered p-n heterojunction structures, the VB and CB edge position of the p-type is above that of the n-type one, which creates a built-in electric field (BEF) when the p-type comes into contact with the n-type. The BEF on p-n photoactive materials with a staggered band gap structure for RZBs possesses multifunction benefits: it supports photogenerated electron-hole pair separation, suppresses photogenerated electron-hole recombination, and improves the photogenerated electrons injection/extraction kinetics used to enhance the redox reaction of RZBs during charge/discharge cycles.

Recent studies have demonstrated that graphitic carbon nitride ($\text{g-C}_3\text{N}_4$), which has a strong adsorption range focusing on ultraviolet-visible (UV-Vis) and a band gap of 2.70 eV, is an efficient, low-cost alternative to Pt/C and $\text{IrO}_2/\text{RuO}_2$ for the bifunctional electrocatalysis of ORR/OER [25]. It has been employed in batteries, photochemical splitting of water, and metal-free heterogeneous catalysis of various organic reactions [26–30]. However, n-type $\text{g-C}_3\text{N}_4$ still suffers from limited absorption of visible light, swift recombination of photogenerated electron-hole pairs, and deficient electrochemical stability [31], etc. To simultaneously enhance the efficiency and durability of the bifunctional catalyst, the metal-organic framework (MOF) has been considered as a favorable candidate owing to its encouraging bifunctional ORR/OER property, photoelectrocatalytic potential, and catalytic stability [32]. However, MOF derivatives such as carbonization of MOFs that pyrolyzed at high-temperature associate with severe decomposed organic linkers with a very low mass yield of catalyst [33]. The zeolitic imidazolate framework-67 (ZIF-67) is a promising conductive MOF with a broad range of UV-Vis-near-infrared (NIR) absorption ability and a band gap of 1.98 eV [34]; as a potential photoactive air-cathode, it has drawn increased attention owing to its extended visible light absorption ability and improved catalytic performance [35,36].

In this study, we developed a photoactive bifunctional air-electrocatalyst with a staggered p-n heterojunction band gap structure, comprising n-type $\text{g-C}_3\text{N}_4$ and p-type copper-doped ZIF-67 (CuZIF-67) composite (named as CZ), to accelerate sluggish OER/ORR processes via a durable structure and stable long-cycle-life performance for photo-enhanced RZBs. This catalyst has three main advantages: (1) a suitable band gap, which ensures wide-range light absorption in the UV-Vis-NIR region, and stimulates more electrons to participate in ORR/OER electrocatalytic activity; (2) a staggered bandgap structure and a BEF at the p-n junction of CZ, which improves electron-hole pairs separation efficiency, lowers overpotential, and enhances battery performance; and (3) a high concentration of pyrrolic-N groups in the cathode material, resulting in the excellent electrochemical durability of RZBs during charge/discharge cycles.

2. Experimental section

2.1. Synthesis of $\text{g-C}_3\text{N}_4/\text{CuZIF-67}$ composite

$\text{g-C}_3\text{N}_4$ was synthesized from calcinating melamine at 550 °C for 4 h

at a heating rate of 5 °C min^{-1} . Cobalt nitrate hexahydrate $\text{Co}(\text{NO}_3)_2$ (970 mg) and copper nitrate hexahydrate $\text{Cu}(\text{NO}_3)_2$ (90 mg) were added in deionized (DI) water (10 mL) to form a solution. 2-Methylimidazole (4.25 g) was dissolved in DI water (15 mL) and added in the mixed solution of $\text{Co}(\text{NO}_3)_2$ and $\text{Cu}(\text{NO}_3)_2$. Next, 0.5 g of as-prepared $\text{g-C}_3\text{N}_4$ was put into the solution and stirred for 20 min, and then moved into a Teflon-lined stainless-steel autoclave (50 mL) and maintained at 110 °C for 24 h. The obtained purple precipitates were acquired through centrifuging and washed with ethanol several times. Finally, $\text{g-C}_3\text{N}_4/\text{CuZIF-67}$ composite was obtained by drying the resulting purple precipitates at 60 °C for 24 h and was named as CZ. CuZIF-67 was prepared by a similar procedure except with the addition of $\text{g-C}_3\text{N}_4$ to the suspension. To explore the optimized condition of CZ, CZ was pyrolyzed at 400 °C in an N_2 environment for 2 h at a heating rate of 5 °C min^{-1} and was named CZ-P. The main role of CZ-P is to investigate major factors related to the long-term cycling stability performance test of the photo-enhanced rechargeable zinc-air batteries (RZBs).

2.2. Physical and chemical characterizations of catalyst-samples

The morphologies and structures of the as-synthesized samples were obtained using an FEI Tecnai F20 G2 Transmission Electron Microscope (TEM) and Energy Dispersive X-Ray Analysis (EDX) operated at 200 kV. X-ray diffraction (XRD) patterns were acquired on an Ultima IV diffractometer (Rigaku corp.) using $\text{Cu K}\alpha$ radiation ($\lambda = 0.15406$ nm) with a scanning 2θ range of 5°–50°. X-ray photoelectron spectroscopy (XPS) tests were carried out on a PHI 5000 VersaProbe (Ulvac-phi) with $\text{Al K}\alpha$ radiation ($h\nu = 1486.6$ eV). UV-Vis absorption spectra of the as-prepared samples were achieved on a UV-Vis spectrophotometer (Shimadzu UV2450) from 200 to 800 nm wavelength at room temperature. BaSO_4 was used as the reflectance standard. Thermogravimetric analysis analyses of prepared samples (~10 mg) were executed using a TA Instruments SDT-Q600 at a heating rate of 10 °C min^{-1} under 100 mL min^{-1} N_2 .

2.3. Electrochemical measurements of ORR and OER

Electrochemical tests were carried out on a VMP3 electrochemical workstation (Bio-Logic) with a three-electrode configuration at ambient temperature. A platinum wire was applied as the counter electrode, and a Hg/HgO in 1.0 mol L^{-1} NaOH solution was employed as the reference electrode. The working electrode was assembled by utilizing a catalyst link on a glassy carbon rotating ring disk electrode (RRDE) with inner and outer diameters of 5 and 7 mm, respectively. The inks for the catalytic layer were prepared by dispersing 10 mg of active materials (containing 3 mg of carbon black) in the mixture solution, which including 600 μL DI water, 350 μL ethanol, and 50 μL 5.0 wt% Nafion solution. After 1 h of sonication, 4 μL of the ink was drop-cast onto the glassy carbon RRDE to make a uniform catalyst layer. Mott-Schottky analysis was performed in 0.5 M Na_2SO_4 with an electrochemical impedance spectroscopy (EIS) test frequency of 1 kHz under dark conditions. Electrocatalytic ORR/OER activity was measured in O_2 -saturated 0.1 mol L^{-1} KOH solution at a scan rate of 10 mV s^{-1} with a rotation speed of 1600 rpm under dark conditions and illumination with a solar simulator (PEC-L01 with 150 W xenon lamp, Peccell Technologies, Inc., 100 mW cm^{-2}) equipped with an AM 1.5 G filter. The onset potential of the ORR process was defined as the potential where the current density achieved 0.1 mA cm^{-2} . All the potentials $E_{(\text{Hg}/\text{HgO})}$ were calibrated and converted into the reversible hydrogen electrode potential $E_{(\text{RHE})}$ according to Eq. 1.

$$E_{(\text{RHE})} = E_{(\text{Hg}/\text{HgO})} + 0.059 \cdot \text{pH} + 0.14 \quad (1)$$

The electron transfer number (n) was determined with an RRDE at 10 mV s^{-1} scan rate and rotating speed of 1600 rpm. n was then calculated using Eq. 2, where i_r is the ring current, i_d is the disk current,

and N is the current collection efficiency (0.424).

$$n = 4 \frac{i_d}{i_d + i_r/N} \quad (2)$$

2.4. Assemblies and tests of photo-enhanced rechargeable zinc-air batteries

The cathode ink was prepared with catalyst, polyvinylidene fluoride, and carbon black in a ratio of 7 (54.0 mg): 1 (7.7 mg): 2 (15.4 mg) in the *N*-methyl-2-pyrrolidone solution (0.5 mL) under ball milling for 0.5 h. The photoactive cathode was obtained by dropping 9.26 μL of the as-prepared ink (average catalyst loading of 1 mg cm^{-2}) drop-casted carbon paper with an area of 1 cm^2 , and then by drying the ink-coated carbon paper in the oven at 60 $^{\circ}\text{C}$ for 24 h. A Zn plate (200 μm thickness) was used as the anode. In addition, the two electrodes were parallel settled in the electrolyte 6.0 mol L^{-1} KOH + 0.2 mol L^{-1} Zn(Ac)₂ with a distance of 1 cm.

The electrochemical performance of photo-enhanced RZBs was investigated using a home-built beaker cell and an RZB reactor. For the beaker cell, O₂ was bubbled into the solution for at least 30 min before testing so that the electrolyte remained in an O₂-saturated condition. The 1-sunlight light irradiated the surface of the air cathode through the side of the transparent beaker cell. For the RZBs reactor, the exposed area of the air cathode was 1 cm^2 . The air cathode was illuminated with a solar simulator (PEC-L01 with 150 W xenon lamp, Peccell Technologies, Inc., 100 mW cm^{-2}) equipped with an AM 1.5 G filter. The distance between the light source and air cathode was fixed, and the measured light irradiance was 1-sunlight illumination.

The tests of the beaker cell and reactor were conducted on a VMP3 electrochemical workstation at ambient temperature. Galvanostatic discharge and charge cycling were tested using the recurrent galvanostatic pulse technique at a constant current density of 2 mA cm^{-2} with each cycle (10 min discharging followed by 10 min charging, 20 min for each cycle). The current densities of each electrode were normalized to

the effective surface area of the air cathode. The specific capacity was computed based on the discharge current (I), test period (t), and the weight of consumed zinc (w_{Zn}) according to Eq. (3).

$$\text{Specific capacity}(\text{mAhg}^{-1}) = \frac{I \times t}{w_{\text{Zn}}} \quad (3)$$

3. Results and discussion

3.1. Physicochemical structure and properties of g-C₃N₄/CuZIF-67 composite

The CZ comprising CuZIF-67 and g-C₃N₄ was synthesized via hydrothermal methods, as shown in Fig. 1a. The structure and morphology of the as-synthesized CZ from TEM analysis are shown in Fig. 1b. The as-synthesized CZ with elements of C, N, Co, Cu, and O shows that a polyhedron of CuZIF-67 with an average size of $\sim 1 \mu\text{m}$ was assembled on the surface of the lamellar structure of g-C₃N₄ because of the hydrogen bond, and this weakened the covalent bond between g-C₃N₄ layers to form a hybrid heterostructure through hydrothermal reaction [37]. The XPS survey spectra of CZ further demonstrate the existence of C, N, Co, Cu, and O, as shown in Fig. S1a. In terms of crystallography, as indicated in the XRD spectra (Fig. 1c), CZ possesses intact crystal parameters of CuZIF-67 and g-C₃N₄. Sharp peaks at 7.4 $^{\circ}$ (011), 12.7 $^{\circ}$ (112), and 18.0 $^{\circ}$ (222) for 2 theta values of CuZIF-67 and CZ confirm the high degree of crystallinity [38]; the small broad peak at 27.6 $^{\circ}$ for CZ corresponds to the (002) of g-C₃N₄ [27]. The abovementioned outcomes further manifest in the close interface between g-C₃N₄ and CuZIF-67; the close contact of the interface could promote the movement of photo-generated carriers at the interface [39]. To investigate the impact of the contact interface and structural integrity of the CuZIF-67 and g-C₃N₄ on ORR/OER catalytic performance and the durability of CZ, the CZ-P pyrolyzed at 400 $^{\circ}\text{C}$ for 2 h was used for comparison.

The light-harvesting nature and optical band gap energy of g-C₃N₄, CuZIF-67, CZ, and CZ-P were obtained through UV-Vis absorption

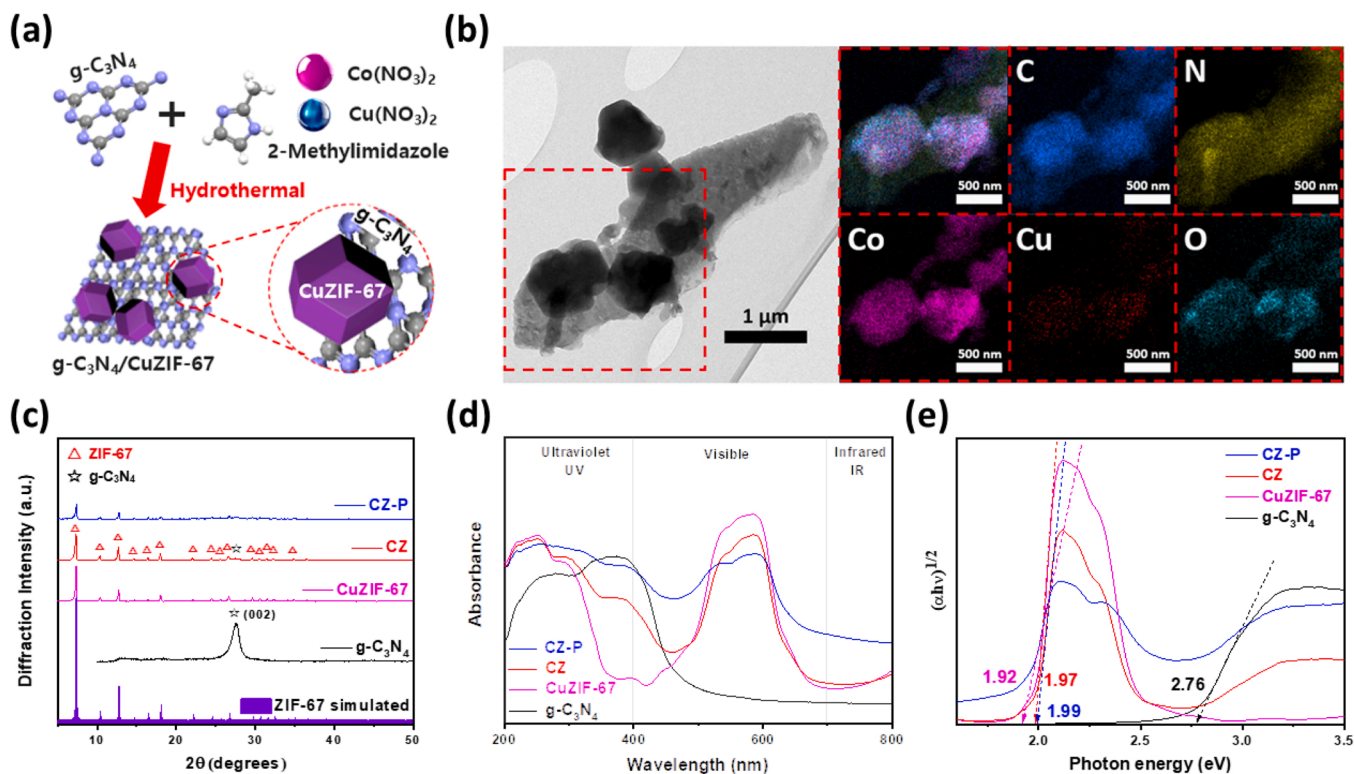


Fig. 1. Preparation and basic characteristics of CZ. (a) Schematic preparation and (b) TEM images with elemental distributions in the red rectangle marked area for CZ. (c) XRD patterns, (d) ultraviolet-visible spectra, and (e) Tauc plots for g-C₃N₄, CuZIF-67, CZ, and CZ-P. (Note: CZ: g-C₃N₄/CuZIF-67; CZ-P: pyrolyzed CZ).

spectra in the spectral wavelength range of 200–800 nm. As displayed in Fig. 1d, g-C₃N₄ mainly absorbs the light from the UV region with an absorption edge of 375 nm. The absorption edge of CuZIF-67 absorbs the light from UV across the visible range up to 646 nm. The absorption region of CZ shows the combination of the spectral feature of g-C₃N₄ and CuZIF-67, as expected. In comparison with g-C₃N₄, the maximum absorption wavelength of CZ was redshifted, owing to the interaction between g-C₃N₄ and CuZIF-67 at the interface, which indicates that CZ alters the electronic structure of the catalyst on the surface and lower the forbidden bandwidth. Besides, the absorption peak intensity of CZ improved in the region of ~400 nm compared with that of CuZIF-67, meaning that the light-absorbing ability of CZ is enhanced for a wide range of light absorption utilizations. Compared with CZ, the absorption intensity of CZ-P was increased in the UV–Vis–NIR spectra. To understand the physical mechanism of the above light absorption phenomenon, as shown in Fig. 1e, the band gap was acquired by deducing the linear region near the onset of the optical absorption edge to the photon energy axis. According to the Tauc equation for direct band gap: $ah\nu = B(h\nu - E_g)^2$, which α is the linear absorption coefficient, h is Planck's constant, ν is the frequency of light, B is a proportionality constant, and E_g is the optical band gap [40]. From Tauc plots of $(ah\nu)^{1/2}$ versus $h\nu$ (photon energy), the obtained band gap values (Fig. S1b) of g-C₃N₄, CuZIF-67, CZ, and CZ-P were 2.76, 1.97, 1.99, and 1.92 eV, respectively. Compared with g-C₃N₄, the gap widths of CZ and CZ-P were significantly reduced owing to the presence of CuZIF-67, which provides an appropriate structural basis for promoting more photogenerated electrons and holes to improve electrocatalytic efficiency [41]. The band gap of CZ-P (1.92 eV) is smaller than that of CZ (1.99 eV), which implies that CZ-P may possess improved photocatalytic efficiency compared with CZ. However, from the XRD results, the crystallinity of CZ-P is lower than that of CZ because of the initial thermal decomposition of the ZIF structure, which may cause instability in the electrochemical process. Based on the thermogravimetric analysis result of g-C₃N₄ and CuZIF-67 in Fig. S1c, typical weight loss under 100 °C is because of the desorption of physisorbed water. No obvious weight loss was observed for g-C₃N₄ and CuZIF-67 in the region between 100 and 400 °C; significant weight loss for CuZIF-67 could be detected at 400 °C and above owing to the decomposition of the ZIF structure [42,43].

To quantitatively determine the semiconducting parameters of the g-C₃N₄, CuZIF-67, and CZ, Mott–Schottky analysis was applied to calculate the flat band potential by measuring the differential capacity of the electric double layer located at the semiconductor/electrolyte interface. Mott–Schottky plots are considered to be a graph of C^{-2} as a function of applied potential where C is the overall capacitance of the interfacial double layer as determined by electrochemical impedance spectroscopy measurements. The flat band potential is obtained from the intercept of the linear part of the Mott–Schottky plot with the potential (Y -axis). As shown in Figs. S2a and S2b, g-C₃N₄ and CuZIF-67 show positive and negative slopes, reflecting n -type and p -type semiconductors, respectively [44]. Furthermore, the flat band potentials of g-C₃N₄ and CuZIF-67 calculated by deducing the intercept of the straight region were -0.21 and 1.19 V versus reversible hydrogen electrode potential (RHE), respectively. Here, the flat band potential is reckoned to be the Fermi level (E_f) of each semiconductor [45,46]. The CB of n -type g-C₃N₄ was more negative around 0.2 V compared with its Fermi level, namely, $E_{CB} = E_f - 0.2$ V = -0.41 V [47,48]. Subsequently, based on the relationship $E_{VB} = E_{CB} + E_g$, the valence band of g-C₃N₄ was ~ 2.35 V versus RHE, which is consistent with the results of a previous work [49]. Similarly, E_{VB} of the p -type CuZIF-67 is usually 0.2 V more positive than its Fermi level, namely, $E_{VB} = E_f + 0.2$ V = 1.39 V. Based on the relationship $E_{CB} = E_{VB} - E_g$, its E_{CB} was approximately -0.58 V versus RHE. The energy band structures and the corresponding electrochemical potentials of g-C₃N₄ and CuZIF-67 before contact are summarized in Fig. S2c and Table S1, based on the reference standard that 0 V versus RHE equals -4.45 eV versus vacuum level [39,50]. It is worth pointing out that the Mott–Schottky curve exhibits a typical inverted “V-shape”

appearance for CZ, which confirms the existence of the p - n heterojunction (Fig. S2d) [51,52].

3.2. Photo-enhanced ORR/OER performance for rechargeable zinc-air batteries

To investigate the bifunctional photoelectrocatalytic performance of the materials, the linear sweep voltammetry (LSV) of ORR/OER was evaluated using a three-electrode electrochemical system under dark and light illumination conditions. As shown in Fig. 2, both the OER and ORR activities and the onset potential were boosted by the simulated solar light illumination. During the ORR process (Fig. 2a), the CZ electrode showed an onset potential of 0.80 V vs RHE under illumination, which is 10 mV higher than that in dark. Concurrently, the limiting current density of CZ also increased from 3.60 to 4.07 mA cm⁻² at 0.2 V vs RHE ($\sim 13.0\%$ increment) compared with dark conditions. Besides, the CZ electrocatalyst also showed an enhanced onset potential compared with the g-C₃N₄ (0.75 V), CuZIF-67 (0.71 V) under the light. The Tafel plots (Fig. 2b) reveal that CZ had a Tafel value of 80 mV dec⁻¹ under light, which is also smaller than that of the electrode under dark conditions, implying that faster ORR kinetics occurred during illumination [53]. As seen in Fig. S3a, the electron transfer number (n) for CZ under the light was 3.6 from the RRDE measurements (Fig. S3b) which is higher than that (3.2) in the dark condition. CZ exhibits a higher electron transfer number under light irradiation, which means improved selectivity of the 4-electron reaction in cathode could promote the efficiency of ORR performance [54–58]. Regarding OER activity (Fig. 2c), the CZ electrode exhibited a small overpotential (η) of 410 mV at a current density of 10 mA cm⁻² under light irradiation based on the equilibrium potential of 1.23 V vs. RHE and was more favorably active than that (460 mV) in the dark environment. Upon light irradiation, the OER current density of CZ drastically increased, for instance, from 22.6 to 29.8 mA cm⁻² at a voltage of 1.8 V ($\sim 31.9\%$ increment). CZ also showed reduced overpotential compared with solitary g-C₃N₄ and outperformed CuZIF-67 in the OER process for both light/dark conditions, as expected. The photocurrent increased linearly with the increasing voltage, which is higher than that of the dark condition. The above-mentioned results indicate that CZ is an effective photo-active ORR/OER-bifunctional electrocatalyst in the aqueous electrolyte as it combines the advantages of the g-C₃N₄ in the ORR process and CuZIF-67 in the OER process under solar illumination.

Considering that ORR and OER are crucial steps in the charging and discharging processes of RZBs, CZ is highly promising for photo-enhanced RZBs. The galvanostatic charge-discharge profiles of the RZBs based on homemade beaker cell design (Fig. S4a) using CZ as cathode under light and dark conditions are shown in Fig. 2d. At a current density of 2 mA cm⁻², the charge and discharge voltage gap of the RZBs under light illumination was 0.82 V vs. Zn, which is smaller than that under dark conditions (0.14 V vs. Zn); this further proves that CZ is a practical photo-active bifunctional electrocatalyst for RZBs. Moreover, the reduced potential gap is directly revealed in the promoted round-trip efficiency of RZBs under solar light irradiation. Besides, the specific discharge capacity under visible light is 781.7 mAh g_{zn}⁻¹ at a current density of 10 mA cm⁻² (Fig. S4b), which is higher than the capacity under dark conditions (731.9 mAh g_{zn}⁻¹) when normalized to the mass of consumed Zn.

The cycling performances of g-C₃N₄-, CuZIF-67-, and CZ-based cathodes for RZBs are shown in Fig. 2e. In dark conditions, RZBs based on CZ showed slightly improved discharging voltage compared with CuZIF-67 owing to the existence of the g-C₃N₄. Concurrently, the charging performance of the RZBs based on CZ showed an advantageous charging voltage compared with g-C₃N₄ owing to the existence of the CuZIF-67. After running in the dark for 3 h, the CZ showed much improved discharging voltage under illumination compared with that under the dark conditions. In detail, after light illumination for more than 5 h, the charging voltage of CZ (1.94 V) was more efficient than

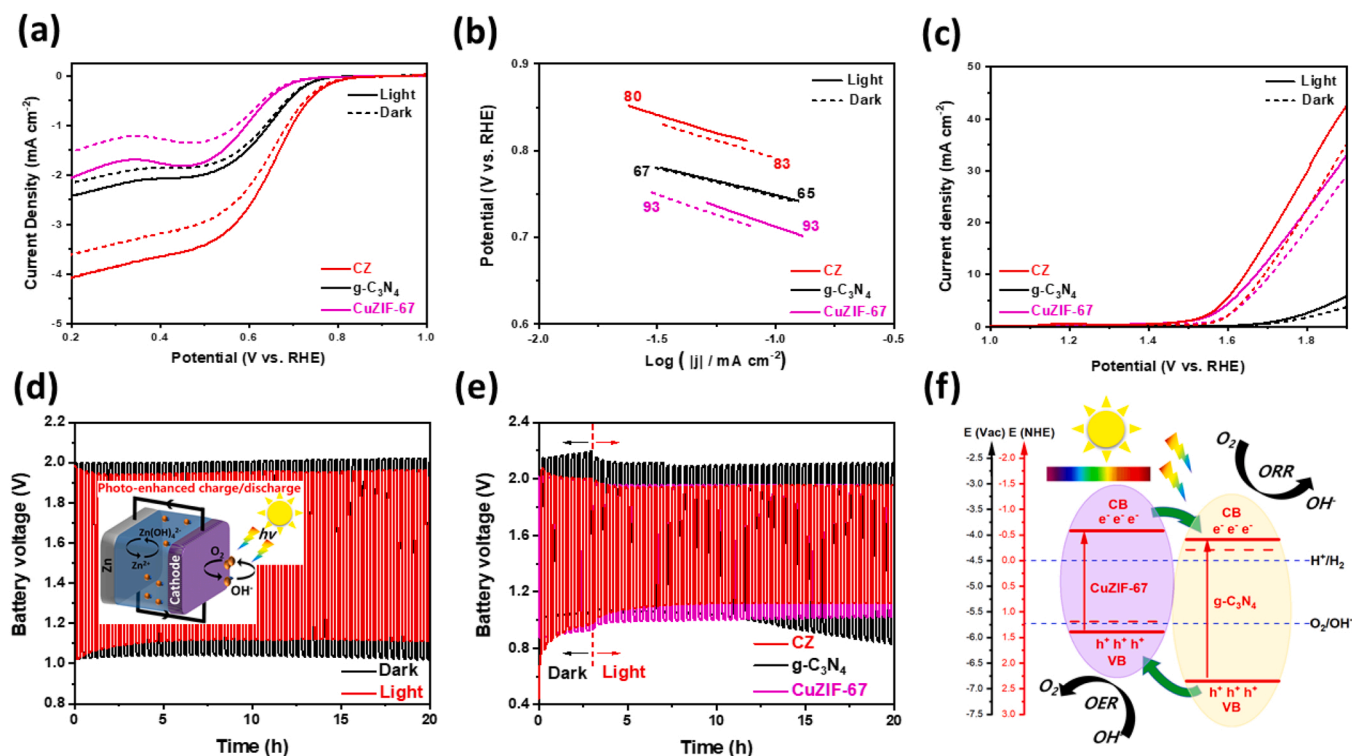
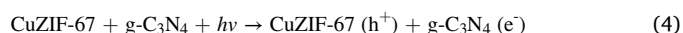


Fig. 2. Photoelectrocatalytic properties of CZ and photo-enhanced performance of rechargeable zinc-air batteries. (a) Linear sweep voltammetry (LSV) of oxygen reduction reaction (ORR), (b) Tafel plots, and (c) LSV of oxygen evolution reaction (OER) for CZ, g-C₃N₄, and CuZIF-67 catalysts in O₂-saturated 0.1 mol L⁻¹ KOH solution at a rotation speed of 1600 rpm with a scan rate of 10 mV s⁻¹ with and without light illumination. (The digital numbers represent the Tafel slope values). (d) Galvanostatic charge-discharge profile of the rechargeable zinc-air batteries with beaker cell design illustrated in the inset image using CZ as cathode under light illumination and dark conditions at 2 mA cm⁻². (e) Comparison between galvanostatic charge-discharge plots of CZ, g-C₃N₄, and CuZIF-67 under dark and light illumination conditions at 2 mA cm⁻². (f) Working mechanism of CZ with the staggered p-n heterojunction for photo-enhanced ORR and OER in aqueous electrolytes.

that of CuZIF-67 (1.96 V) and g-C₃N₄ (2.09 V), as shown in Fig. S4c, which means that the CuZIF-67 in the CZ composite is the main contributor to the photo-enhanced OER under light conditions. Meanwhile, the discharging voltage of CZ (1.12 V) is also more productive than those of g-C₃N₄ (1.05 V) and CuZIF-67 (1.00 V), which indicates that g-C₃N₄ in the CZ composite has a greater contribution to photo-enhanced ORR under light conditions. It is important to point out here that photo-enhanced RZB performance (owing to synergistic effects from the suitable bandgap width, staggered bandgap structure, and local built-in electric field at its p-n heterojunction) leads to higher ORR and OER electrocatalytic activities compared with single p- and n-type catalysts with photo-enhanced charging and discharging abilities.

Fig. 2f shows the working mechanism of a photo-enhanced CZ-cathode based on the staggered p-n heterojunction. Under light illumination, the VB of p-type CuZIF-67 is hit by photons, which creates photogenerated electron-hole pairs. The photogenerated electrons are then excited from the VB to CB of CuZIF-67, leaving behind the photo-generated holes in the CB. The BEF was naturally created at the CuZIF-67/g-C₃N₄ junction, with the positive and negative BEF polar formed at the g-C₃N₄ and CuZIF-67 regions, respectively [59]. Supported by this BEF, the excited photogenerated electrons at the CB of the p-type CuZIF-67 are transferred to and accumulated at the CB of the n-type g-C₃N₄. The corresponding reaction is shown in Eq. 4. These photogenerated electrons then participate in the ORR process (Eq. 5) as additional electrons to reduce O₂ and enhance ORR electrocatalytic activity during the RZB discharge process [24,60]. Meanwhile, the photogenerated holes accumulated at the VB of p-type CuZIF-67 then participate in the OER process (Eq. 6) to oxidize OH⁻ and enhance OER electrocatalytic activity during the RZB charge process [24,60]. Therefore, the ORR and OER performances of photo-enhanced RZBs with CZ-cathodes is expected to be synchronously promoted under light

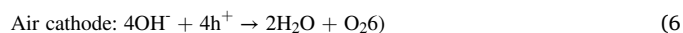
illumination compared with that under dark conditions because the p-n effect boosts the separation of photogenerated carriers. Subsequently, the additional electrons and holes converted from the light participate in the discharging and charging processes, respectively [37,61].



Discharge process.



Charge process.



3.3. Durability study of photo-enhanced zinc-air batteries

Cyclic durability is another critical indicator to evaluate the practicability of photo-enhanced RZBs. As shown in Fig. 3a, CZ-P exhibited advantageous charge/discharge performance compared with CZ at the beginning of the cycling test under light illustration owing to a reduced band gap that improving electrocatalytic efficiency. However, the round-trip efficiency of CZ-P deteriorated faster than that of CZ after 7 h of light irradiation, because of the thermal decomposition of the ZIF structure of CZ-P at 400 °C. In contrast, CZ demonstrated stable performance after 20 h operation in dark/light conditions. Therefore, the structural integrity of the ZIF structure may be critical for the prolonged lifetime of photo-enhanced RZBs. To investigate the reasons why CZ possesses preferred durability, XPS analysis was carried out to evaluate the elemental composition in the surface regions of CZ and CZ-P. In general, the functional groups that originate from the C and N

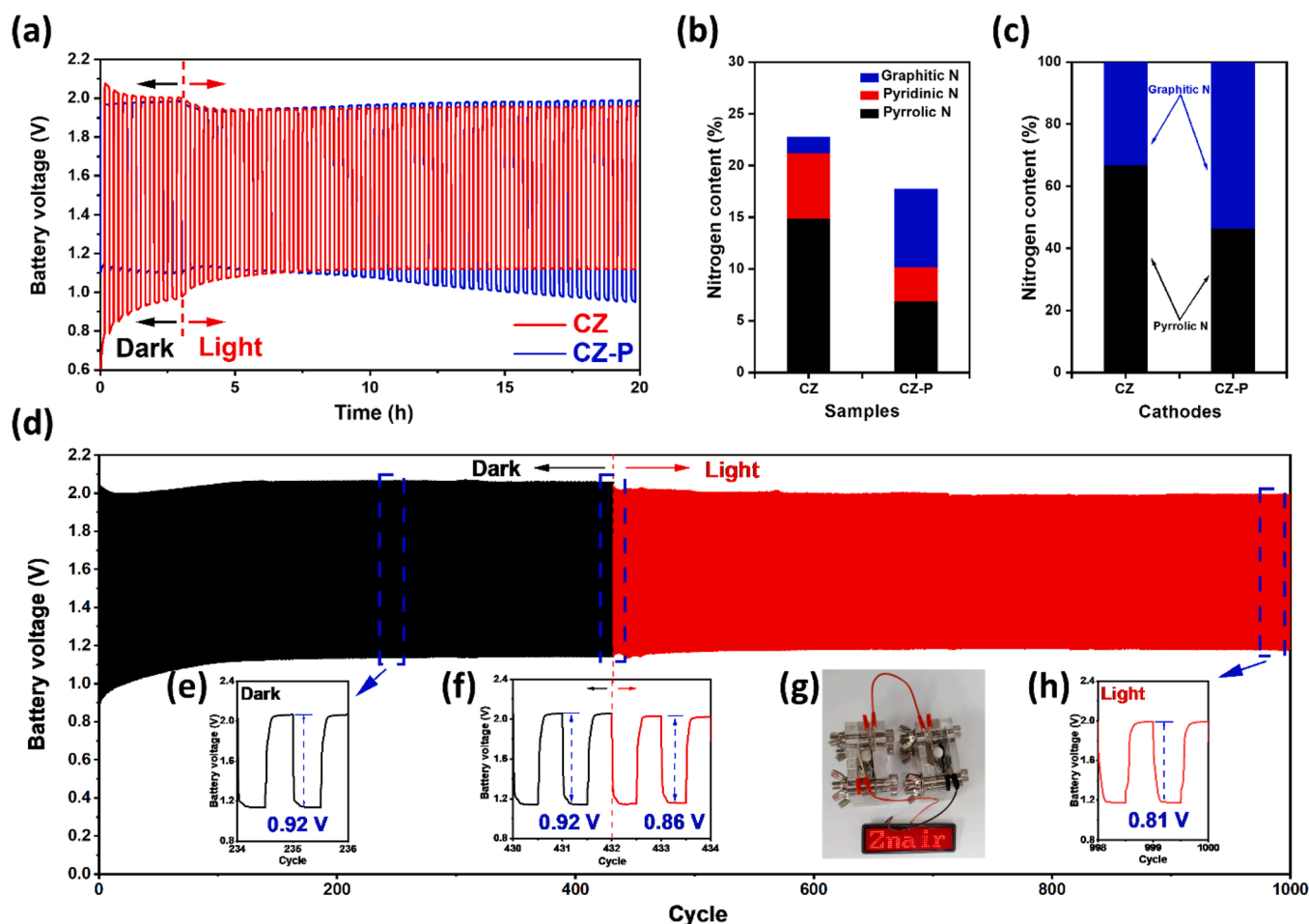


Fig. 3. Durability study of photo-enhanced Zn-air batteries. (a) Cycling-stability comparison of the RZBs based on between CZ and CZ-P at 2 mA cm^{-2} under light illumination and in dark. Corresponding nitrogen contents of (b) CZ and CZ-P active materials before the cycling test and (c) CZ and CZ-P based cathode after the cycling measurements. (d) Long-term galvanostatic charge-discharge profile with zoomed (e) dark, (f) dark-light shifting, and (h) light regions of the CZ-based zinc-air battery at a current density of 2 mA cm^{-2} for up to 1000 cycles. (g) LED screen powered by two CZ-based RZBs in series.

remarkably affect the electronic structure/binding affinity of carbon-based materials [62,63]. The different types of N in CZ and CZ-P were examined from the high-resolution spectra of N 1s (Fig. S5a), which are deconvoluted into three peaks: pyridinic N (398.5 eV), pyrrolic N (398.8 eV), and graphitic N (400.4 eV) [63]. With higher pyrolysis temperature for CZ-P, the proportions of graphitic N increased with increasing temperature, and the concentration of pyrrolic N decreased because it decomposed at higher pyrolysis temperature. Pyridinic N and graphitic N are active sites for the OER and ORR as previously reported [62,64]. Pyridinic N has a lone electron pair in the plane of the carbon matrix that could facilitate the electron-donating ability to improve the electrochemical onset potential; graphitic N affects the limiting current density in the ORR process [65]. Considering that the concentration of the pyridinic N and graphitic N on the surface of CZ-P is higher than that on the surface of CZ, it is reasonable that CZ-P possesses improved electrochemical efficiency at the beginning of the cycling performance. Meanwhile, the percentage of pyrrolic N decreased from 14.6% (CZ) to 7.0% (CZ-P) with increased pyrolysis temperature, as shown in Fig. 3b. Many studies have demonstrated that an abundance of pyrrolic N effectively lowers carbon corrosion and results in superior catalyst stability during the electrochemical process [66,67]. Therefore, the excellent durability of RZBs based on CZ as the air cathode may reflect the high concentration of pyrrolic N and integrated ZIF structure.

To validate the excellent stability of CZ because of the pyrrolic N-rich groups, XPS analysis was also performed to investigate the surface composition and chemical-state transformation of CZ and CZ-P after

long cycling performance. Fig. S5b and S5c present the XPS survey spectra of the cathode of RZBs based on CZ and CZ-P before and after cycling, respectively. The XPS spectrum of CZ and CZ-P before cycling shows peaks at binding energies of 285, 399, 532, 688, and 782 eV, corresponding to C 1s, N 1s, O 1s, F 1s, and Co 2p, respectively. Significantly, the signal of C 1s is dominant before and after cycling owing to the carbon fiber paper employed as a substrate for the cathode of photo-enhanced RZBs. The emergence of the F 1s peak in the survey spectra is attributed to the use of polyvinylidene fluoride binder in the preparation of the CZ and CZ-P cathodes. The peak intensity of each element was lower than before the test owing to the loss of active materials during the RZB cycling and also the cleaning process for cathode reclamation after cycling. A detailed examination of the high-resolution N 1s spectra after cycling measurements further confirmed that the higher percentage of pyrrolic N benefits the durability of CZ on the cathode (Fig. S5d). The N 1s spectra of CZ and CZ-P after the cycling test can be deconvoluted into two main peaks located at 400.2 eV for graphitic N and 398.8 eV for pyrrolic N; these peak positions agree with the active materials before the test. Interestingly, the pyridinic N peak can hardly be detected from the surface of the cathode after long cycling, which may suggest that pyridinic N makes a limited contribution to the durability of CZ. Besides, as the corresponding N contents of CZ and CZ-P after cycling (Fig. 3c), the pyrrolic N concentration of CZ (66.6%) on the surface of the cathode was twice that of graphitic N (33.3%) after the test. As a comparison, the pyrrolic N concentration of CZ-P (46.4%) on the surface of the cathode was even lower than the graphitic N (53.6%)

after cycling. CZ possessed a much higher percentage of pyrrolic N than CZ-P after long cycling performance, which further confirms the assumption that the excellent durability of CZ reflects the higher concentration of pyrrolic N on the surface of the cathode.

Based on the promising photo-enhanced RZB performance shown in the beaker cell design, a proof-to-concept application was carried out to demonstrate its practicality in a reactor design that does not necessitate an O₂-saturated environment. The RZB reactor was assembled similarly to the beaker cell design except with the air cathode exposed to the air directly. As shown in Fig. S6a, RZBs based on CZ cathodes have an open-circuit potential of 1.42 V under light irradiation, which is superior to dark conditions (1.37 V). The ameliorated charge and discharge polarization curves of the RZBs using CZ as a photo-active cathode material under illumination can be observed in Fig. S6b. To further ascertain the practicability of the RZBs in the real environment, two CZ-based RZB reactors in series delighted an LED screen, as shown in Fig. 3g. The rechargeability of the CZ cathode was evaluated by galvanostatic charge-discharge at a current density of 2 mA cm⁻² (Fig. 3d), accompanied by each cycle being discharged for 10 min and then charged for 10 min. First, the cycling test was carried out for 6 days in the dark; the voltage gap between the discharging and charging of CZ-based RZB was 0.92 V, with a stable round-trip efficiency of 55% (Fig. 3e). Then, the cathode of the reactor was illuminated by a simulated solar light after 6 days; the voltage gap of CZ decreased to 0.86 V after 40 min of irradiation (Fig. 3f). After more than 8 days of 1-sunlight irradiation (Fig. 3h), the charging and discharging voltages of CZ were 1.99 and 1.18 V, respectively, with a voltage gap of 0.81 V and round-trip efficiency of 60%, demonstrating its practical application value with superior cycling stability (1000 cycles) and an outstanding lifetime (> 334 h). The excellent energy efficiency of the photo-enhanced RZBs employing CZ as the air cathode results in an outstanding performance in comparison with the recently pre-reported air electrodes (Table S2). The enhanced RZB performance owing to the CZ electrode is excited by absorbing light, and simultaneously producing photoelectrons in the conduction band and photogenerated holes in the valence band. Then, the photocatalytic evolution of O₂ was promoted owing to the photogenerated carriers could easily react with OH⁻ at the interface. Simultaneously, electrons are excited to a high energy state from VB to CB and generate electron-hole pairs when the photoelectrode is irradiated with light. The above results suggest that CZ holds great potential for photo-enhanced energy conversion and storage application owing to the stable bifunctional electrode materials, which have a wide-range solar light absorption ability and a carefully designed p-n heterojunction on the air cathode of RZBs.

4. Conclusions

In this study, a photoactive bifunctional air cathode catalyst with p-n heterojunction, comprising n-type g-C₃N₄ and p-type CuZIF-67, was designed for photo-enhanced RZBs. The optimized CZ air cathode possesses a 1.99 eV bandwidth and a staggered band gap structure, which ensures a broad light absorption UV-Vis-NIR region, and stimulates more electrons to participate in ORR/OER processes with lowering overpotential and improved photoelectrocatalytic kinetics. Moreover, the BEF caused by the p-n junction of CZ additionally promotes ORR/OER electrocatalytic activity (~13.0% increment of ORR limiting current density and ~31.9% increment of OER current density at 1.8 V) and eventually enhances the efficiency of RZBs (the voltage gap was significantly decreased by 14% with simulated solar light irradiation). In addition, the CZ with integrated structure and high concentration of pyrrolic N leads to exciting electrochemical durability during long-term charge/discharge cycles. In summary, the photo-enhanced RZB based on the CZ bifunctional catalyst exhibits good round-trip efficiency of 60% (2 mA cm⁻²) with a significantly decreased voltage gap (from 0.92 to 0.81 V) after 1000 cycles, under simulated solar light irradiation.

CRedit authorship contribution statement

Ren Ren: Investigation, Conceptualization, Data curation, Methodology, Project administration, Formal analysis, Writing – original draft. **Guicheng Liu:** Conceptualization, Methodology, Resources, Supervision, Writing – review & editing. **Ji Young Kim:** Data curation, Formal analysis. **Ryanda Enggar Anugrah Ardhi:** Writing – review & editing. **Minh Xuan Tran:** Formal analysis. **Woochul Yang:** Formal analysis. **Joong Kee Lee:** Supervision, Project administration, Methodology, Writing – review & editing.

Declaration of Competing Interest

The authors declare that they have no known competing financial interests or personal relationships that could have appeared to influence the work reported in this paper.

Acknowledgements

This research was supported by the Brain Pool program funded by the Ministry of Science and ICT through the National Research Foundation of Korea (2019H1D3A1A01069779). This work is also supported by KIST Institutional Program (2E31863).

Appendix A. Supporting information

Supplementary data associated with this article can be found in the online version at doi:10.1016/j.apcatb.2022.121096.

References

- [1] N. Xu, J.A. Wilson, Y.-D. Wang, T. Su, Y. Wei, J. Qiao, X.-D. Zhou, Y. Zhang, S. Sun, Flexible self-supported bi-metal electrode as a highly stable carbon- and binder-free cathode for large-scale solid-state zinc-air batteries, *Appl. Catal. B Environ.* 272 (2020) 118953–118963, <https://doi.org/10.1016/j.apcatb.2020.118953>.
- [2] T. Zhou, N. Zhang, C. Wu, Y. Xie, Surface/interface nanoengineering for rechargeable Zn-air batteries, *Energy Environ. Sci.* 13 (2020) 1132–1153, <https://doi.org/10.1039/c9ee03634b>.
- [3] M.Q. Liu, L.Y. Yang, H. Liu, A. Amine, Q.H. Zhao, Y.L. Song, J.L. Yang, K. Wang, F. Pan, Artificial solid-electrolyte interface facilitating dendrite-free zinc metal anodes via nanowetting effect, *ACS Appl. Mater. Interfaces* 11 (2019) 32046–32051, <https://doi.org/10.1021/acsami.9b11243>.
- [4] W. Lao-Atiman, S. Olaru, A. Arpornwichanop, S. Kheawhom, Discharge performance and dynamic behavior of refuellable zinc-air battery, *Sci. Data* 6 (2019) 168–175, <https://doi.org/10.1038/s41597-019-0178-3>.
- [5] J. Zhang, Q.X. Zhou, Y.W. Tang, L. Zhang, Y.G. Li, Zinc-air batteries: are they ready for prime time? *Chem. Sci.* 10 (2019) 8924–8929, <https://doi.org/10.1039/c9sc04221k>.
- [6] Y.T. Sun, X.R. Liu, Y.M. Jiang, J. Li, J. Ding, W.B. Hu, C. Zhong, Recent advances and challenges in divalent and multivalent metal electrodes for metal-air batteries, *J. Mater. Chem. A* 7 (2019) 18183–18208, <https://doi.org/10.1039/c9ta05094a>.
- [7] C. Zhang, H. Yang, D. Zhong, Y. Xu, Y. Wang, Q. Yuan, Z. Liang, B. Wang, W. Zhang, H. Zheng, T. Cheng, R. Cao, A yolk-shell structured metal-organic framework with encapsulated iron-porphyrin and its derived bimetallic nitrogen-doped porous carbon for an efficient oxygen reduction reaction, *J. Mater. Chem. A* 8 (2020) 9536–9544, <https://doi.org/10.1039/d0ta00962h>.
- [8] Z.M. Zhao, J.W. Zhao, Z.L. Hu, J.D. Li, J.J. Li, Y.J. Zhang, C. Wang, G.L. Cui, Long-life and deeply rechargeable aqueous Zn anodes enabled by a multifunctional brighter-inspired interphase, *Energy Environ. Sci.* 12 (2019) 1938–1949, <https://doi.org/10.1039/c9ee00596j>.
- [9] Y. Qian, Z. Hu, X. Ge, S. Yang, Y. Peng, Z. Kang, Z. Liu, J.Y. Lee, D. Zhao, A metal-free ORR/OER bifunctional electrocatalyst derived from metal-organic frameworks for rechargeable Zn-air batteries, *Carbon* 111 (2017) 641–650, <https://doi.org/10.1016/j.carbon.2016.10.046>.
- [10] H. Yang, B. Wang, H. Li, B. Ni, K. Wang, Q. Zhang, X. Wang, Trimetallic sulfide mesoporous nanospheres as superior electrocatalysts for rechargeable Zn-air batteries, *Adv. Energy Mater.* 8 (2018) 1801839–1801847, <https://doi.org/10.1002/aenm.201801839>.
- [11] L. An, Z. Zhang, J. Feng, F. Lv, Y. Li, R. Wang, M. Lu, R.B. Gupta, P. Xi, S. Zhang, Heterostructure-promoted oxygen electrocatalysis enables rechargeable zinc-air battery with neutral aqueous electrolyte, *J. Am. Chem. Soc.* 140 (2018) 17624–17631, <https://doi.org/10.1021/jacs.8b09805>.
- [12] C. Lai, J. Fang, X. Liu, M. Gong, T. Zhao, T. Shen, K. Wang, K. Jiang, D. Wang, In situ coupling of NiFe nanoparticles with N-doped carbon nanofibers for Zn-air batteries driven water splitting, *Appl. Catal. B Environ.* 285 (2021) 119856–119863, <https://doi.org/10.1016/j.apcatb.2020.119856>.

- [13] C. Tomon, S. Sarawutanukul, S. Duangdangchote, A. Krittayathananon, M. Sawangphruk, Photoactive Zn-air batteries using spinel-type cobalt oxide as a bifunctional photocatalyst at the air cathode, *Chem. Commun.* 55 (2019) 5855–5858, <https://doi.org/10.1039/c9cc01876j>.
- [14] Y. Chen, W. Zhang, Z. Zhu, L. Zhang, J. Yang, H. Chen, B. Zheng, S. Li, W. Zhang, J. Wu, F. Huo, Co nanoparticles combined with nitrogen-doped graphitic carbon anchored on carbon fibers as a self-standing air electrode for flexible zinc-air batteries, *J. Mater. Chem. A* 8 (2020) 7184–7191, <https://doi.org/10.1039/d0ta00793e>.
- [15] X. Liu, Y. Yuan, J. Liu, B. Liu, X. Chen, J. Ding, X. Han, Y. Deng, C. Zhong, W. Hu, Utilizing solar energy to improve the oxygen evolution reaction kinetics in zinc-air battery, *Nat. Commun.* 10 (2019) 4767–4776, <https://doi.org/10.1038/s41467-019-12627-2>.
- [16] T. Wang, Z. Kou, S. Mu, J. Liu, D. He, I.S. Amiin, W. Meng, K. Zhou, Z. Luo, S. Chaemchuen, F. Verpoort, 2D dual-metal zeolitic-imidazolate-framework-(ZIF)-derived bifunctional electrodes with ultrahigh electrochemical properties for rechargeable zinc-air batteries, *Adv. Funct. Mater.* 28 (2018) 1705048–1705056, <https://doi.org/10.1002/adfm.201705048>.
- [17] S. Sarawutanukul, C. Tomon, S. Duangdangchote, N. Phattarasapukun, M. Sawangphruk, Rechargeable photoactive Zn-air batteries using NiCo₂S₄ as an efficient bifunctional photocatalyst towards OER/ORR at the cathode, *Batter. Supercaps* 3 (2020) 541–547, <https://doi.org/10.1002/batt.201900205>.
- [18] K. Wang, Z. Mo, S. Tang, M. Li, H. Yang, B. Long, Y. Wang, S. Song, Y. Tong, Photo-enhanced Zn-air batteries with simultaneous highly efficient in situ H₂O₂ generation for wastewater treatment, *J. Mater. Chem. A* 7 (2019) 14129–14135, <https://doi.org/10.1039/c9ta04253a>.
- [19] J. Lv, S.C. Abbas, Y. Huang, Q. Liu, M. Wu, Y. Wang, L. Dai, A photo-responsive bifunctional electrocatalyst for oxygen reduction and evolution reactions, *Nano Energy* 43 (2018) 130–137, <https://doi.org/10.1016/j.nanoen.2017.11.020>.
- [20] S.P. Adhikari, Z.D. Hood, H. Wang, R. Peng, A. Krall, H. Li, V.W. Chen, K.L. More, Z. Wu, S. Geyer, A. Lachgar, Enhanced visible light photocatalytic water reduction from a g-C₃N₄/SrTa₂O₆ heterojunction, *Appl. Catal. B Environ.* 217 (2017) 448–458, <https://doi.org/10.1016/j.apcatb.2017.05.092>.
- [21] J. Low, J. Yu, M. Jaroniec, S. Wageh, A.A. Al-Ghamdi, Heterojunction photocatalysts, *Adv. Mater.* 29 (2017) 1601694–1601713, <https://doi.org/10.1002/adma.201601694>.
- [22] Z.-F. Huang, J. Song, X. Wang, L. Pan, K. Li, X. Zhang, L. Wang, J.-J. Zou, Switching charge transfer of C₃N₄/W₁₈O₄₉ from type-II to Z-scheme by interfacial band bending for highly efficient photocatalytic hydrogen evolution, *Nano Energy* 40 (2017) 308–316, <https://doi.org/10.1016/j.nanoen.2017.08.032>.
- [23] Y. Jia, S. Li, J. Gao, G. Zhu, F. Zhang, X. Shi, Y. Huang, C. Liu, Highly efficient (BiO)₂CO₃-BiO_{2-x} graphene photocatalysts: Z-Scheme photocatalytic mechanism for their enhanced photocatalytic removal of NO, *Appl. Catal. B Environ.* 240 (2019) 241–252, <https://doi.org/10.1016/j.apcatb.2018.09.005>.
- [24] J. Su, G.D. Li, X.H. Li, J.S. Chen, 2D/2D heterojunctions for catalysis, *Adv. Sci.* 6 (2019) 1801702–1801720, <https://doi.org/10.1002/advs.201801702>.
- [25] J.E. Park, M.-J. Kim, M.S. Lim, S.Y. Kang, J.K. Kim, S.-H. Oh, M. Her, Y.-H. Cho, Y.-E. Sung, Graphitic carbon nitride-carbon nanofiber as oxygen catalyst in anion-exchange membrane water electrolyzer and rechargeable metal-air cells, *Appl. Catal. B Environ.* 237 (2018) 140–148, <https://doi.org/10.1016/j.apcatb.2018.05.073>.
- [26] J. Zhang, F. Ren, M. Deng, Y. Wang, Enhanced visible-light photocatalytic activity of a g-C₃N₄/BiVO₄ nanocomposite: a first-principles study, *Phys. Chem. Chem. Phys.* 17 (2015) 10218–10226, <https://doi.org/10.1039/c4cp06089j>.
- [27] C. Han, L. Ge, C. Chen, Y. Li, X. Xiao, Y. Zhang, L. Guo, Novel visible light induced Co₃O₄-g-C₃N₄ heterojunction photocatalysts for efficient degradation of methyl orange, *Appl. Catal. B Environ.* 147 (2014) 546–553, <https://doi.org/10.1016/j.apcatb.2013.09.038>.
- [28] P. Suyana, P. Ganguly, B.N. Nair, A.P. Mohamed, K.G.K. Warriar, U.S. Hareesh, Co₃O₄-C₃N₄ p-n nano-heterojunctions for the simultaneous degradation of a mixture of pollutants under solar irradiation, *Environ. Sci. Nano* 4 (2017) 212–221, <https://doi.org/10.1039/c6en00410e>.
- [29] W. Zhang, W. Shi, H. Sun, Y. Shi, H. Luo, S. Jing, Y. Fan, F. Guo, C. Lu, Fabrication of ternary CoO/g-C₃N₄/Co₃O₄ nanocomposite with p-n-p type heterojunction for boosted visible-light photocatalytic performance, *J. Chem. Technol. Biotechnol.* 96 (2021) 1854–1863, <https://doi.org/10.1002/jctb.6703>.
- [30] Y. Huang, B. Chen, J. Duan, F. Yang, T. Wang, Z. Wang, W. Yang, C. Hu, W. Luo, Y. Huang, Graphitic carbon nitride (g-C₃N₄): an interface enabler for solid-state lithium metal batteries, *Angew. Chem. Int. Ed.* 59 (2020) 3699–3704, <https://doi.org/10.1002/anie.201914417>.
- [31] J. Liang, X. Yang, Y. Wang, P. He, H. Fu, Y. Zhao, Q. Zou, X. An, A review on g-C₃N₄ incorporated with organics for enhanced photocatalytic water splitting, *J. Mater. Chem. A* 9 (2021) 12898–12922, <https://doi.org/10.1039/d1ta00890k>.
- [32] Z. Liang, H. Guo, G. Zhou, K. Guo, B. Wang, H. Lei, W. Zhang, H. Zheng, U.P. Apfel, R. Cao, Metal-organic-framework-supported molecular electrocatalysis for the oxygen reduction reaction, *Angew. Chem. Int. Ed.* 60 (2021) 8472–8476, <https://doi.org/10.1002/anie.202016024>.
- [33] J. Li, Z. Meng, D.J.L. Brett, P.R. Shearing, N.T. Skipper, I.P. Parkin, S. Gadipelli, High-performance zinc-air batteries with scalable metal-organic frameworks and platinum carbon black bifunctional catalysts, *ACS Appl. Mater. Interfaces* 12 (2020) 42696–42703, <https://doi.org/10.1021/acsami.0c10151>.
- [34] D. Saliba, M. Ammar, M. Rammal, M. Al-Ghoul, M. Hmadeh, Crystal growth of ZIF-8, ZIF-67, and their mixed-metal derivatives, *J. Am. Chem. Soc.* 140 (2018) 1812–1823, <https://doi.org/10.1021/jacs.7b11589>.
- [35] C. Gu, J. Li, J.-P. Liu, H. Wang, Y. Peng, C.-S. Liu, Conferring supramolecular guanosine gel nanofiber with ZIF-67 for high-performance oxygen reduction catalysis in rechargeable zinc-air batteries, *Appl. Catal. B Environ.* 286 (2021) 119888–119897, <https://doi.org/10.1016/j.apcatb.2021.119888>.
- [36] Y. Zhao, Q. Lai, J. Zhu, J. Zhong, Z. Tang, Y. Luo, Y. Liang, Controllable construction of core-shell polymer/zeolitic imidazolate frameworks fiber derived heteroatom-doped carbon nanofiber network for efficient oxygen electrocatalysis, *Small* 14 (2018) 1704207–1704215, <https://doi.org/10.1002/smll.201704207>.
- [37] Y. Meng, L. Zhang, H. Jiu, Q. Zhang, H. Zhang, W. Ren, Y. Sun, D. Li, Construction of g-C₃N₄/ZIF-67 photocatalyst with enhanced photocatalytic CO₂ reduction activity, *Mater. Sci. Semicond. Process.* 95 (2019) 35–41, <https://doi.org/10.1016/j.mssp.2019.02.010>.
- [38] M. Wang, J. Liu, C. Guo, X. Gao, C. Gong, Y. Wang, B. Liu, X. Li, G.G. Gurzadyan, L. Sun, Metal-organic frameworks (ZIF-67) as efficient cocatalysts for photocatalytic reduction of CO₂: the role of the morphology effect, *J. Mater. Chem. A* 6 (2018) 4768–4775, <https://doi.org/10.1039/c8ta00154e>.
- [39] Y. Zhang, Z. Jin, Boosting photocatalytic hydrogen evolution achieved by NiS_x coupled with g-C₃N₄/ZIF-67 heterojunction, *J. Phys. Chem. C* 123 (2019) 18248–18263, <https://doi.org/10.1021/acs.jpcc.9b04695>.
- [40] E.M. Chen, L. Williams, A. Olvera, C. Zhang, M. Zhang, G. Shi, J.T. Heron, L. Qi, L. J. Guo, E. Kioupakis, P.F.P. Poudeu, Sustainable p-type copper selenide solar material with ultra-large absorption coefficient, *Chem. Sci.* 9 (2018) 5405–5414, <https://doi.org/10.1039/c8sc00873f>.
- [41] H. Park, D. Amaranatha Reddy, Y. Kim, R. Ma, J. Choi, T.K. Kim, K.-S. Lee, Zeolitic imidazolate framework-67 (ZIF-67) rhombic dodecahedrons as full-spectrum light harvesting photocatalyst for environmental remediation, *Solid State Sci.* 62 (2016) 82–89, <https://doi.org/10.1016/j.solidstatesciences.2016.10.018>.
- [42] S. Lai, L. Xu, H. Liu, S. Chen, R. Cai, L. Zhang, W. Theis, J. Sun, D. Yang, X. Zhao, Controllable synthesis of CoN₃ catalysts derived from Co/Zn-ZIF-67 for electrocatalytic oxygen reduction in acidic electrolytes, *J. Mater. Chem. A* 7 (2019) 21884–21891, <https://doi.org/10.1039/c9ta08134h>.
- [43] L. Tao, C.-Y. Lin, S. Dou, S. Feng, D. Chen, D. Liu, J. Huo, Z. Xia, S. Wang, Creating coordinatively unsaturated metal sites in metal-organic-frameworks as efficient electrocatalysts for the oxygen evolution reaction: Insights into the active centers, *Nano Energy* 41 (2017) 417–425, <https://doi.org/10.1016/j.nanoen.2017.09.055>.
- [44] C. Jiang, S.J.A. Moniz, A. Wang, T. Zhang, J. Tang, Photoelectrochemical devices for solar water splitting - materials and challenges, *Chem. Soc. Rev.* 46 (2017) 4645–4660, <https://doi.org/10.1039/c6cs00306k>.
- [45] A. Hankin, J.C. Alexander, G.H. Kelsall, Constraints to the flat band potential of hematite photo-electrodes, *Phys. Chem. Chem. Phys.* 16 (2014) 16176–16186, <https://doi.org/10.1039/c4cp00096j>.
- [46] S. Harrison, M. Hayne, Photoelectrolysis using type-II semiconductor heterojunctions, *Sci. Rep.* 7 (2017) 11638–11648, <https://doi.org/10.1038/s41598-017-11971-x>.
- [47] W. Guo, S. Shu, T. Zhang, Y. Tao, Y. Xie, X. Liu, An inorganic-organic hybrid polymer cocatalyst for photoelectrochemical water oxidation with dual functions of accelerating kinetics and improving charge transfer, *CCS Chem.* (2021) 969–978, <https://doi.org/10.31635/ccschem.021.202100785>.
- [48] P. Wang, D. Li, J. Chen, X. Zhang, J. Xian, X. Yang, X. Zheng, X. Li, Y. Shao, A novel and green method to synthesize CdSe quantum dots-modified TiO₂ and its enhanced visible light photocatalytic activity, *Appl. Catal. B Environ.* 160–161 (2014) 217–226, <https://doi.org/10.1016/j.apcatb.2014.05.032>.
- [49] M. Han, H. Wang, S. Zhao, L. Hu, H. Huang, Y. Liu, One-step synthesis of CoO/g-C₃N₄ composites by thermal decomposition for overall water splitting without sacrificial reagents, *Inorg. Chem. Front.* 4 (2017) 1691–1696, <https://doi.org/10.1039/c7qi00380c>.
- [50] D. Liu, D. Chen, N. Li, Q. Xu, H. Li, J. He, J. Lu, ZIF-67-derived 3d hollow mesoporous crystalline Co₃O₄ wrapped by 2D g-C₃N₄ nanosheets for photocatalytic removal of nitric oxide, *Small* 15 (2019) 1902291–1902301, <https://doi.org/10.1002/smll.201902291>.
- [51] J. Qian, C. Shen, J. Yan, F. Xi, X. Dong, J. Liu, Tailoring the electronic properties of graphene quantum dots by p doping and their enhanced performance in metal-free composite photocatalyst, *J. Phys. Chem. C* 122 (2017) 349–358, <https://doi.org/10.1021/acs.jpcc.7b08702>.
- [52] F. Meng, J. Li, S.K. Cushing, M. Zhi, N. Wu, Solar hydrogen generation by nanoscale p-n junction of p-type molybdenum disulfide/n-type nitrogen-doped reduced graphene oxide, *J. Am. Chem. Soc.* 135 (2013) 10286–10289, <https://doi.org/10.1021/ja404851s>.
- [53] Y. Chen, R. Ren, Z. Wen, S. Ci, J. Chang, S. Mao, J. Chen, Superior electrocatalysis for hydrogen evolution with crumpled graphene/tungsten disulfide/tungsten trioxide ternary nanohybrids, *Nano Energy* 47 (2018) 66–73, <https://doi.org/10.1016/j.nanoen.2018.02.023>.
- [54] W. Xia, J. Zhu, W. Guo, L. An, D. Xia, R. Zou, Well-defined carbon polyhedrons prepared from nano metal-organic frameworks for oxygen reduction, *J. Mater. Chem. A* 2 (2014) 11606–11613, <https://doi.org/10.1039/c4ta01656d>.
- [55] M. Peng, Y. Zhao, J. Lan, Y. Qiao, Y. Tan, Self-standing 3D nanoporous Ag₂Al with abundant surface oxygen species facilitating oxygen electroreduction for efficient hybrid Zn battery, *J. Energy Chem.* 58 (2021) 345–354, <https://doi.org/10.1016/j.ijechem.2020.10.015>.
- [56] D. Du, S. Zhao, Z. Zhu, F. Li, J. Chen, Photo-excited oxygen reduction and oxygen evolution reactions enable a high-performance Zn-air battery, *Angew. Chem. Int. Ed.* 59 (2020) 18140–18144, <https://doi.org/10.1002/anie.202005929>.
- [57] D. Zhu, Q. Zhao, G. Fan, S. Zhao, L. Wang, F. Li, J. Chen, Photoinduced oxygen reduction reaction boosts the output voltage of a zinc-air battery, *Angew. Chem. Int. Ed.* 58 (2019) 12460–12464, <https://doi.org/10.1002/anie.201905954>.
- [58] Z. Fang, Y. Zhang, X. Hu, X. Fu, L. Dai, D. Yu, Tactile UV- and solar-light multi-sensing rechargeable batteries with smart self-conditioned charge and discharge,

- Angew. Chem. Int. Ed. 58 (2019) 9248–9253, <https://doi.org/10.1002/anie.201903805>.
- [59] X. Chang, T. Wang, P. Zhang, J. Zhang, A. Li, J. Gong, Enhanced surface reaction kinetics and charge separation of p-n heterojunction $\text{Co}_3\text{O}_4/\text{BiVO}_4$ photoanodes, *J. Am. Chem. Soc.* 137 (2015) 8356–8359, <https://doi.org/10.1021/jacs.5b04186>.
- [60] M. Luo, W. Sun, B.B. Xu, H. Pan, Y. Jiang, Interface engineering of air electrocatalysts for rechargeable zinc–air batteries, *Adv. Energy Mater.* 11 (2020) 2002762–2002775, <https://doi.org/10.1002/aenm.202002762>.
- [61] X. Liu, J. Zhang, Y. Dong, H. Li, Y. Xia, H. Wang, A facile approach for the synthesis of Z-scheme photocatalyst ZIF-8/g- C_3N_4 with highly enhanced photocatalytic activity under simulated sunlight, *New J. Chem.* 42 (2018) 12180–12187, <https://doi.org/10.1039/c8nj01782d>.
- [62] Y. Wang, N. Aquino de Carvalho, S. Tan, L.M. Gilbertson, Leveraging electrochemistry to uncover the role of nitrogen in the biological reactivity of nitrogen-doped graphene, *Environ. Sci. Nano* 6 (2019) 3525–3538, <https://doi.org/10.1039/c9en00802k>.
- [63] G. Ma, C. Li, F. Liu, M.K. Majeed, Z. Feng, Y. Cui, J. Yang, Y. Qian, Metal-organic framework-derived $\text{Co}_{0.85}\text{Se}$ nanoparticles in N-doped carbon as a high-rate and long-lifespan anode material for potassium ion batteries, *Mater. Today Energy* 10 (2018) 241–248, <https://doi.org/10.1016/j.mtener.2018.09.013>.
- [64] B. Dahal, S.-H. Chae, A. Muthurasu, T. Mukhiya, J. Gautam, K. Chhetri, S. Subedi, G.P. Ojha, A.P. Tiwari, J.H. Lee, H.-Y. Kim, An innovative synthetic approach for core-shell multiscale hierarchically porous boron and nitrogen codoped carbon nanofibers for the oxygen reduction reaction, *J. Power Sources* 453 (2020) 227883–227893, <https://doi.org/10.1016/j.jpowsour.2020.227883>.
- [65] Z. Lin, X. Qiao, Coral-like Co_3O_4 decorated N-doped carbon particles as active materials for oxygen reduction reaction and supercapacitor, *Sci. Rep.* 8 (2018) 1802–1811, <https://doi.org/10.1038/s41598-018-19347-5>.
- [66] H. Schmies, E. Hornberger, B. Anke, T. Jurzinsky, H.N. Nong, F. Dionigi, S. Kühl, J. Drnec, M. Lerch, C. Cremers, P. Strasser, Impact of carbon support functionalization on the electrochemical stability of Pt fuel cell catalysts, *Chem. Mater.* 30 (2018) 7287–7295, <https://doi.org/10.1021/acs.chemmater.8b03612>.
- [67] L. Zhang, Q. Wang, R. Si, Z. Song, X. Lin, M.N. Banis, K. Adair, J. Li, K. Doyle-Davis, R. Li, L.M. Liu, M. Gu, X. Sun, New insight of pyrrole-like nitrogen for boosting hydrogen evolution activity and stability of Pt single atoms, *Small* 17 (2021) 2004453–2004462, <https://doi.org/10.1002/sml.202004453>.